Rayleigh–Taylor Growth Measurements of 3-D Modulations in a Nonlinear Regime

Introduction

Rayleigh–Taylor (RT)[1,2] instability is of critical importance in inertial confinement fusion (ICF)[3] and astrophysics.[4] In ICF, the RT instability leads to shell disruption and performance degradation of spherically imploding targets.[3] In astrophysics, when a star becomes a supernova, the outer shell is pushed by the inner exploding core and heavy material from the inner core appears in the outer shell because of the RT mixing process.[4] In the linear regime of classical RT instability,[3,5] small initial modulations grow exponentially in time with the growth rate $\gamma = (Akg)^{0.5}$, where k is the modulation wave number, g is the target acceleration, and A is the Atwood number defined as $A = (\rho_h - \rho_l)/(\rho_h + \rho_l)$, where ρ_h and ρ_l are the densities of heavy and light fluids, respectively. Most ICF-related cases involve ablative drive in which the growth rate $\gamma = \alpha(kg)^{0.5} - \beta k V_a$ is stabilized by the ablation term $\beta k V_a$, where V_a is the ablation velocity and α and β are constants.[6,7] This growth rate is an approximation of a more exact formula in Ref. 7. The growth rates of linear RT instability have been measured in both classical[5] and ablative regimes.[8–12] The indication of nonlinearity in RT growth in real space is that the modulations develop into bubbles (penetration of the lighter fluid into the heavier) and spikes (penetration of the heavier fluid into the lighter).[13] In Fourier space, this is equivalent to the harmonics generation of initial fundamental spatial modes. As the RT instability further progresses, the two fluids mix in turbulent and chaotic regimes.[14–17] There are two modeling approaches for nonlinear RT instability: a modal one[18–20] that describes the evolution in Fourier space and a bubble competition and merger that describes instability in real space.[17,21–24] In Fourier space, Haan's model[18] [see Fig. 105.10(a)] predicts that the spectral amplitudes of 3-D, broadband modulations grow exponentially with the RT growth rates of $\gamma(k)$ until they reach the saturation levels[18,25] $S_k = 2/Lk^2$ (L is the size of the analysis

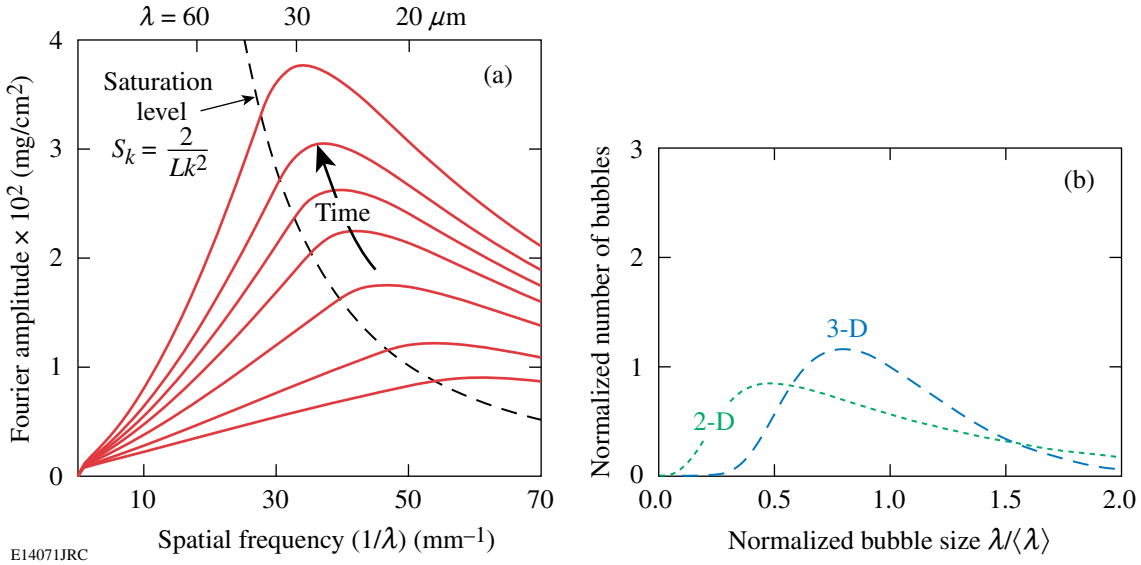

Figure 105.10
(a) Fourier spectra of target areal-density modulations driven by Rayleigh–Taylor instability, as predicted by Haan's model.[18] The dashed line is Haan's saturation level $S_k = 2/Lk^2$ (L = 400 μm is the size of analysis box) multiplied by the calculated target density to be converted to areal density.[25] (b) Bubble size distributions as a function of the bubble size normalized to the average bubble size $\lambda/\langle\lambda\rangle$ as predicted by 2-D (dotted curve) and 3-D (dashed curve) bubble competition models in a self-similar regime.[27]

box), after which they grow linearly in time with the saturation velocities[18,26] $V_s(k) = S_k\gamma(k)$. The short-wavelength modes grow initially most rapidly and quickly saturate at levels S_k while very long-wavelength modes grow more slowly. As a result, the midwavelength modes have the largest growth factors, producing a peak in the spectrum. As the evolution continues, this peak moves to longer wavelengths, as shown in Fig. 105.10(a). Haan's model applies in the weakly nonlinear regime for broadband modulation amplitudes around the saturation levels.[25] In real space, bubble competition models predict that smaller bubbles (with smaller nonlinear velocities) are taken over by larger bubbles (with higher nonlinear velocities) through bubble competition and the bubble merger processes.[17,21–24] As a result, the average size of the modulations shifts to longer wavelengths as the modulations grow. The real-space models predict that the bubble sizes and amplitudes evolve with a self-similar behavior in an advanced nonlinear regime.[24,27,28] The self-similar behavior predicts that the distribution function $f(\lambda/\langle\lambda\rangle)$ of the bubble size normalized to the average bubble size $\lambda/\langle\lambda\rangle$ is constant as the modulation average size and average amplitude grow.[24,27,28] Figure 105.10(b) shows self-similar bubble size distributions predicted by 2-D and 3-D bubble competition models.[24,27] It should be noted here that Haan's model is applicable for broadband initial spectra, which can contain both long and short wavelengths. The bubble competition model is mainly applicable for initial spectra dominated by short wavelengths, whereas long wavelengths are mainly produced by bubble merger processes.[27] This article presents results of nonlinear RT experiments[25,26,28,29] performed over several years on the OMEGA Laser System[30] and shows new results in which planar targets were directly driven by laser light and 3-D broadband modulation growth was measured near nonlinear saturation levels. The initial broadband modulations were dominated by short wavelengths in these experiments; therefore, both real-space (bubble) and Fourier-space models can be used for comparison with experimental data. This article compares measured RT evolution with that predicted by both Fourier- and real-space nonlinear RT models. The experiments with initial broadband modulations dominated by long-wavelengths modes are described elsewhere.[26]

In this article, **Experimental Configuration** (p. 18) describes the experimental configuration and measurement technique. **Experimental Results** are discussed on p. 19 and **Conclusions** are presented on p. 24.

Experimental Configuration

In the experiments, initially smooth, 1-mm-diam CH targets with thicknesses ranging from 20 to 50 μm were driven with 12-ns and 3-ns square pulses at laser intensities of ~5 × 10^{13} W/cm^2 and ~2 × 10^{14} W/cm^2, respectively, on the OMEGA Laser System.[30] The modulation growth was measured with through-foil, x-ray radiography.[29] The backlighter x rays that probe target modulations were imaged by an 8-μm pinhole array onto a framing camera, allowing up to eight images with a temporal resolution of ~80 ps and a spatial resolution of ~10 μm to be captured at different times in each shot.[29] The initial target modulations, used for RT growth measurements, were imprinted by laser-beam nonuniformities created by using standard distributed phase plates[31] (SG8 DPP's) during the first several hundred picoseconds of the drive. Figure 105.11 shows a measured equivalent-target-plane image of the laser beam with the DPP [Fig. 105.11(a)] along with its Fourier spectrum [Fig. 105.11(b)]. The beam with DPP has broadband modulations with spatial frequencies up to ~320 mm^{-1}, corresponding to the smallest spatial size of ~3 μm and an intensity

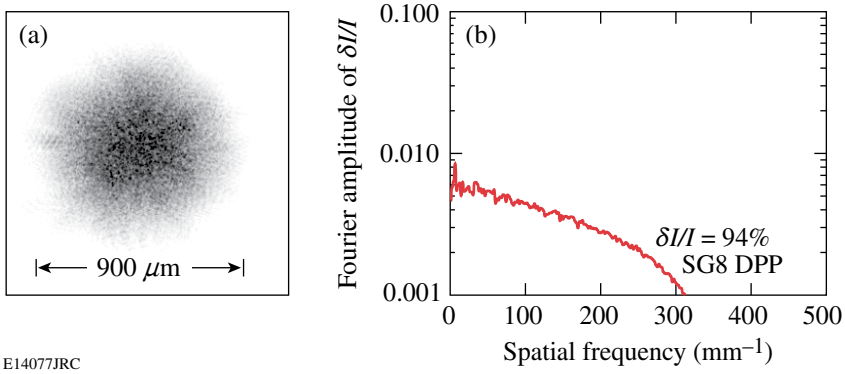

Figure 105.11
(a) The equivalent-target-plane image of the laser beam with a distributed phase plate (SG8 DPP). (b) Fourier spectrum of relative intensity [$\delta I/I$] modulations of the laser beam with a SG8 DPP. The smallest size of intensity modulations in the beam is ~3 μm and it has an intensity modulation σ_{rms} of ~94%.

modulation σ_{rms} of ~94%. The amplitudes of target modulations $a_t(k)$ are proportional to the amplitudes of relative laser modulations[32,33] $a_l(k)$, $a_t(k) = E(k)a_l(k)$, where $E(k) \sim 1/k$ is the imprint efficiency.[33–35] Some experiments used smoothing by spectral dispersion (SSD)[36] and polarization smoothing (PS)[37] to vary the spectrum of target modulations to study the dependence of the RT growth on the initial conditions. Polarization smoothing reduces the modulations of most laser spatial frequencies by a factor[37] of $\sqrt{2}$, while SSD reduces high-spatial frequency modulations more strongly than the low-spatial frequency modulations.[36]

The typical optical-depth (OD) images (obtained by taking a natural logarithm of intensity-converted, framing-camera images) of x-ray radiographs are shown in Fig. 105.12 for an experiment with a 20-μm-thick target driven with a 3-ns square pulse shape.[29] A Weiner filter (based on measured system resolution and noise) was applied to these images to remove noise and deconvolve the system's modulation transfer function to recover target OD modulations.[29] The measured target OD variations are proportional to the variations of target areal density $\delta[\rho R]$; $\delta[\mathrm{OD}(t)] = \mu_{CH}(E)\delta[\rho R(t)]$, where $\mu_{CH}(E)$ is the CH target mass absorption rate at x-ray energy E used for backlighting and t is the time of the measurement. The areal-density $\delta[\rho R(t)]$ modulations were obtained by dividing measured OD modulations by target mass absorption rates. The RT growth of the initial nonuniformities was analyzed in the central parts (with a box size of up to 400 μm) of these images where the average drive is uniform.

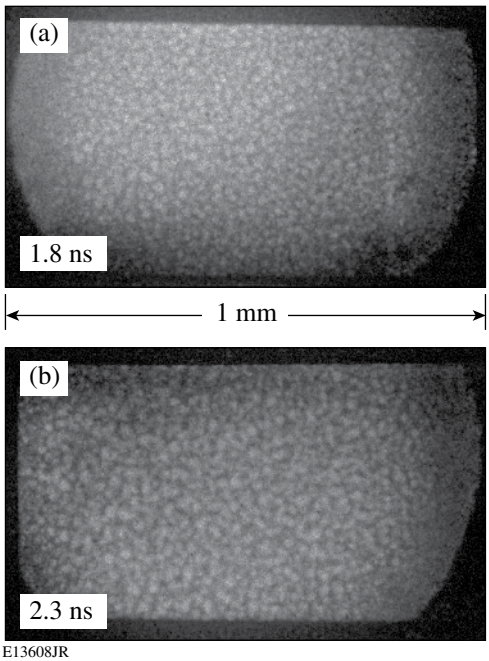

Figure 105.12
X-ray framing-camera images of RT growth modulations measured at (a) 1.8 and (b) 2.3 ns in a 20-μm-thick target driven by a 3-ns laser pulse at an intensity of ~2×10^{14} W/cm^2. Central, 400-μm-square parts of the images were taken for analysis.

As laser light is applied to the target, the pressure created by the target ablation launches a shock wave that compresses the target.[35] Any nonuniformities in the laser drive are imprinted into the target modulations at this time.[32–35] When the shock front reaches the rear surface of the target, it sends the rarefaction wave back to the ablation surface; shortly thereafter, the target begins to accelerate (in these experiments after around 0.5 to 1 ns, depending on target thickness). During the acceleration phase, the ablation-surface modulations grow exponentially because of Rayleigh–Taylor instability.[1–3] At later times these modulations become detectable with our diagnostics as their evolution enters the nonlinear regime. [25,26,28,29]

Experimental Results

Figure 105.13 shows the Fourier spectra of growing target areal-density modulations $\delta[\rho R(t)]$ measured in 20-μm-thick targets [Figs. 105.13(a) and 105.13(b)] and a 40-μm-thick target [Fig. 105.13(c)] driven with a 3-ns square laser drive pulse at an intensity of ~2×10^{14} W/cm^2 (Refs. 25 and 29). The smoothing conditions included DDP's, SSD, and PS on a shot shown in Fig. 105.13(a) and DPP's only on shots in Figs. 105.13(b) and 105.13(c). The dashed lines show Haan's saturation levels[18] (as described in the **Introduction** on p. 17). The smoothing conditions were varied to determine whether the shapes of modulation Fourier spectra in the nonlinear regime depend on the initial conditions. The target thickness was varied to measure the sensitivity of modulation Fourier spectra to drive conditions since target acceleration and growth rates depend on the target thickness. The shapes of the measured spectra are very similar to Haan's model predictions in all shots[25,29] (compare with Fig. 105.10). These shapes are insensitive to initial and drive conditions, as predicted by Haan's model. In the shot with more laser smoothing [Fig. 105.13(a)], the modulations are detected later than in the shot with less smoothing [Fig. 105.13(b)], and the growth is shifted by ~1 ns. In the shot with a 40-μm-thick target [Fig. 105.13(c)], the growth is detected later than with a 20-μm-thick target because of the reduced growth in the thicker target [compare Figs. 105.13(b) and 105.13(c)]. At later times, the measured modulation level becomes comparable with the target thickness and the effects of finite target thickness significantly slow the growth,[29] as shown in Fig. 105.14(a). The amplitudes of short-scale modulations

even decrease toward the end of the drive (~2.8 ns) because of this effect.[29] The measured target images [see Figs. 105.14(b) and 105.14(c)] show that smaller bubbles start to merge as larger bubbles grow during this time. In these earlier 1999 experiments, two questions still remained: (1) Do the bubble-merger processes happen around saturation levels or do they begin in a more deeply nonlinear regime (as it was considered in bubble-competition models)? (2) Is the bubble competition accompanied by a reduction of the short-wavelength modulations [as shown in Fig. 105.14(a)], or is this reduction because of the finite target thickness effects?

To address these questions and to make a connection between Fourier-space and real-space models, new experiments were conducted[26] with thicker targets driven to much higher amplitudes with longer pulses in a deeper nonlinear regime. Figure 105.15 shows examples of the measured images[26] for a shot with a 50-μm-thick target driven by a 12-ns square pulse

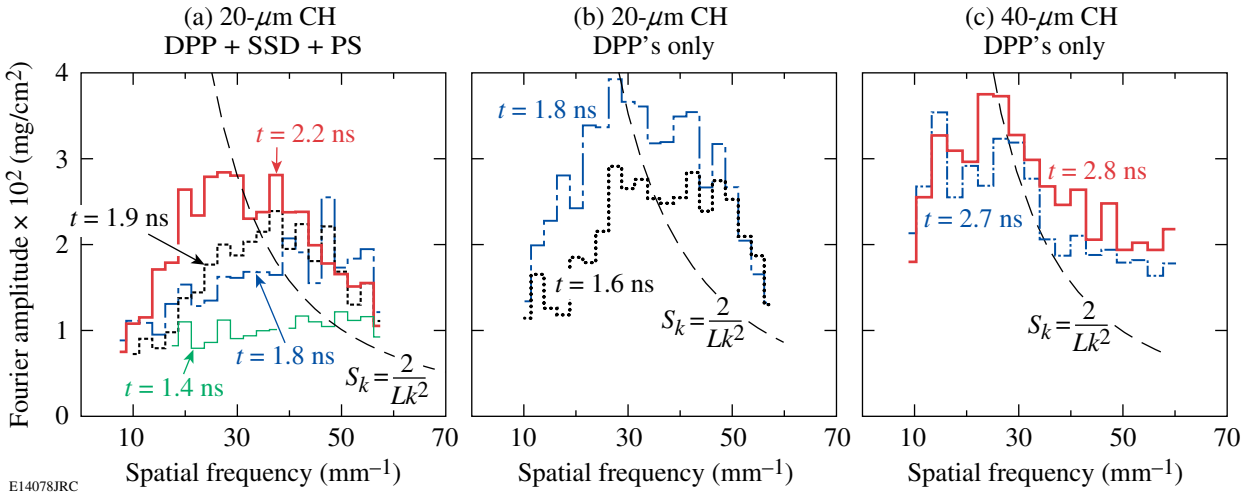

Figure 105.13
Evolution of the azimuthally averaged, areal-density modulation Fourier amplitudes as a function of spatial frequency for shots with 20-μm-thick [(a) and (b)] and 40-μm-thick (c) targets driven by a 3-ns laser pulse at an intensity of ~2×10^{14} W/cm^2 and with beam-smoothing conditions that include DDP's, SSD, and PS (a) and DPP's only [(b) and (c)]. The dashed line is Haan's saturation level $S_k = 2/Lk^2$ ($L = 400$ μm is the size of analysis box) multiplied by the calculated target density to be converted to areal density. The spectral shapes of measured modulations are similar to those predicted by Haan's model and are insensitive to initial and drive conditions.

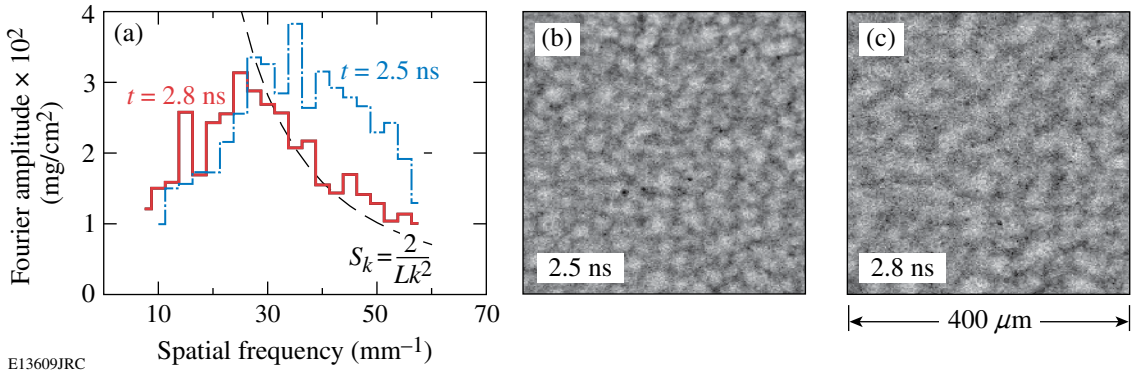

Figure 105.14
(a) Evolution of the azimuthally averaged, areal-density modulation Fourier amplitudes as a function of spatial frequency for the shot with a 20-μm-thick target driven by a 3-ns laser pulse at an intensity of ~2×10^{14} W/cm^2 and with beam-smoothing conditions including DDP's, SSD, and PS measured at 2.5 and 2.8 ns. As the level of target modulations becomes comparable to the target thickness, the modulation growth slows down and is later reversed (at 2.8 ns). The bubble-merger processes are evident from the images measured at (b) 2.5 ns and (c) 2.8 ns.

shape at an intensity of ~5×10^{13} W/cm^2. The beam-smoothing conditions in these experiments included DPP's and PS. As the modulations grow, the average bubble size shifts to longer wavelengths, big bubbles become bigger, and small bubbles disappear, as is evident from the images in Fig. 105.15. Two to three generations of bubbles change (by coalescence events) in these images, allowing clear observations of the bubble competition and merger processes. One can claim that the bubble competition and merger processes occur around saturation levels (and not only in a more advanced, turbulent regime).

Figure 105.16(a) shows examples of Fourier amplitude evolution of areal-density modulations, typical for these experiments.[26] The spectral shapes are very similar to Haan's model predictions; the amplitudes grow to much higher values than those achieved in the 1999 experiments[29] because thicker targets do not limit RT growth at the times of these measurements. The fact that in the 2005 experiments [see Fig. 105.16(a)] there is no reduction in short-wavelength modulations allows one to conclude that the bubble competition is not accompanied by a reduction of the short-wavelength modulations [as shown in

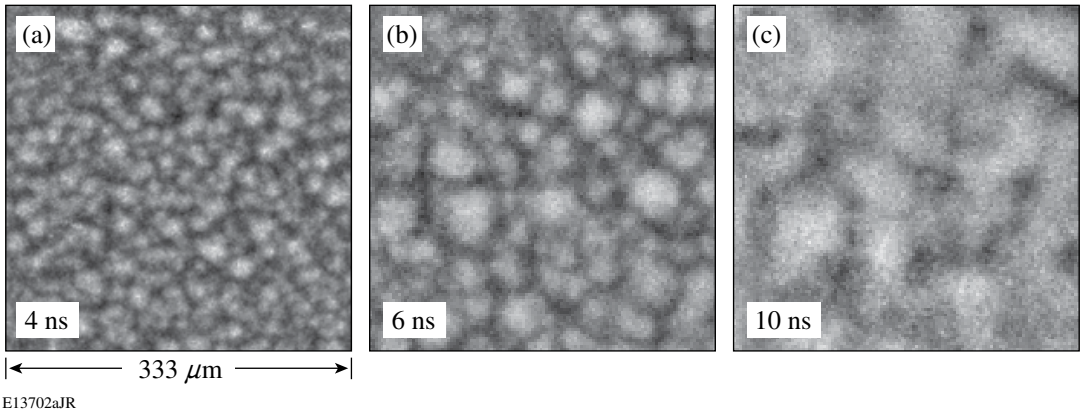

Figure 105.15
Central parts (with the analysis box size of 333 μm) of the x-ray framing-camera images measured at (a) 4 ns, (b) 6 ns, and (c) 10 ns in a 50-μm-thick target driven by a 12-ns laser pulse at an intensity of ~5×10^{13} W/cm^2 from Ref. 26. The bubble merger is evident in the images showing more advanced nonlinear RT evolution measured in thicker targets driven by longer pulses.

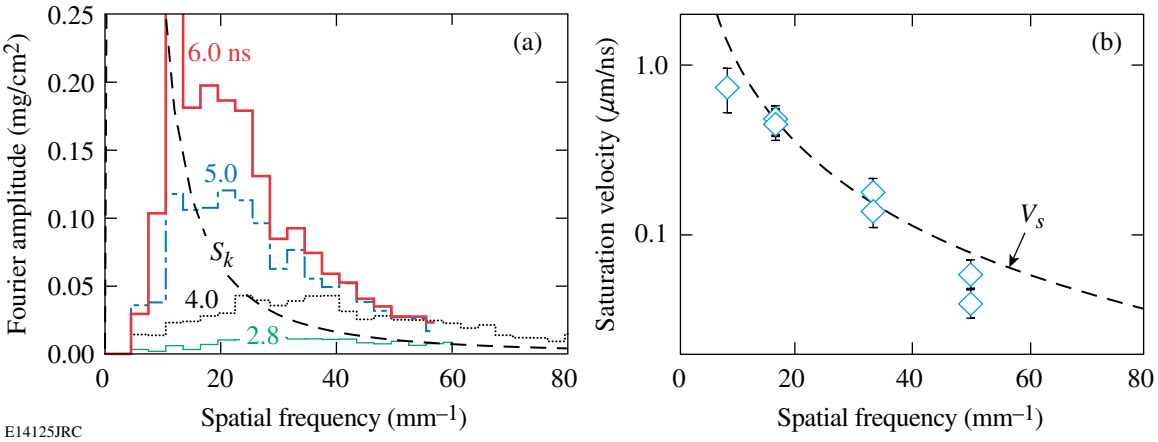

Figure 105.16
(a) Evolution of the azimuthally averaged, areal-density modulation Fourier amplitudes as a function of spatial frequency for shots with 50-μm-thick targets driven by a 12-ns laser pulse at an intensity of ~5×10^{13} W/cm^2 from Ref. 26. The dashed line is Haan's saturation level $S_k = 2/Lk^2$ ($L = 333$ μm is the analysis box size) multiplied by the calculated target density to be converted to areal density. The spectral shapes of the measured modulations are similar to those predicted by Haan's model. (b) Saturation velocities of target modulations measured at spatial frequencies of 8, 17, 33, and 50 mm^{-1} corresponding to spatial wavelengths of 120, 60, 30, and 20 μm from Ref. 26. The dashed line is Haan's saturation velocity $V_s(k) = S_k\gamma(k)$. The measured nonlinear velocities are in excellent agreement with Haan's model predictions.

Fig. 105.14(a)]—this reduction is because of the finite target thickness effects that limited RT growth and prevented clear observation of the bubble competition in the 1999 experiments. Additionally, the fact that the RT growth in the 2005 experiments is not limited by target thickness allows a direct comparison of the measured nonlinear velocities $V_s(k)$ with those predicted by Haan's model,[26] and excellent agreement between the experiments and the model was observed[26] [as shown in Fig. 105.16(b)]. We find it remarkable that this simple model predicts such complicated phenomenon as the nonlinear saturation and the postsaturation growth of the RT instability so accurately in terms of the spectral shapes and nonlinear velocities.

The real-space analysis of the 2005 experiments was based on evolution distributions of the bubble sizes and amplitudes along with the evolution of average bubble size and amplitude.[28] Figure 105.17 shows an example of the measured image with bubble edges superimposed on top of it. The bubble edges were determined using a watershed algorithm.[38] The bubble size λ was calculated using $\lambda = 2(S/\pi)^{0.5}$, where S is the bubble area. The evolution of the distributions of bubble sizes λ [corresponding to images in Figs. 105.14(a) and 105.14(b)] is shown in Fig. 105.18(a). As modulations grow, the number of bubbles decreases while their average size and amplitude increase and the distributions become broader. The measured distributions of bubble sizes were fitted with the normal distributions from which average sizes $\langle\lambda\rangle$ were determined. Figure 105.18(b) shows the normalized distributions [from Fig. 105.18(a)] as functions of normalized bubble size $\lambda/\langle\lambda\rangle$. Bubble size distributions are in the self-similar regime because the normalized distributions do not change in time. The self-similarity of RT growth is explicitly measured in these experiments using the evolution of bubble size distributions, while in earlier simulations and experiments[16,17] the self-similarity was inferred from the growth of the mixing-zone size. The dashed line in Fig. 105.18(b) represents the fit to the experimental data using the normal distribution

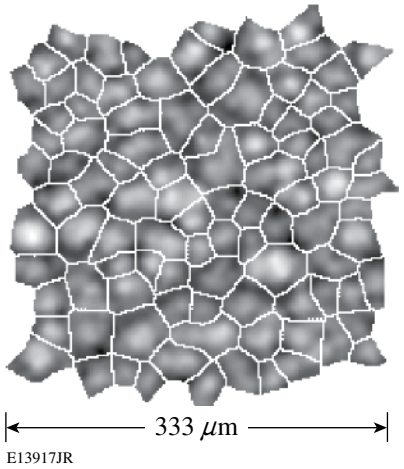

Figure 105.17
An example of the measured image with bubble edges (determined using watershed algorithm[38]) superimposed on top of it.

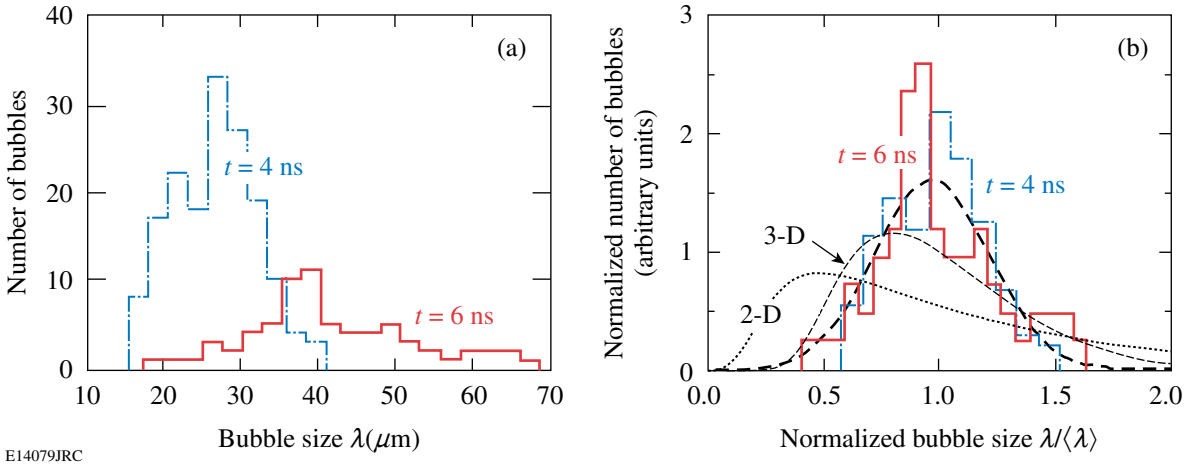

Figure 105.18
(a) Examples of the measured bubble size distributions in the images taken at 4 and 6 ns [images in Figs. 105.15(a), and 105.15(b), respectively] with a 50-μm-thick target driven by a 12-ns laser pulse at an intensity of ~5×10^{13} W/cm^2. (b) Bubble-size distributions, normalized to the total number of bubbles, as a function of the bubble size normalized to the averaged bubble size $\lambda/\langle\lambda\rangle$ for the same 4- and 6-ns images as in (a). The measured bubble distributions are in a self-similar regime because their normalized distributions do not change in time. The thicker dashed line represents a normal distribution fit to the data.

$f_\sigma(\lambda/\langle\lambda\rangle) = \exp\left[-(\lambda/\langle\lambda\rangle - 1)^2 \Big/ 2C_\lambda^2\right] \Big/ \sqrt{2\pi} \cdot C_\lambda$, where C_λ = 0.24±0.01 is the constant determined from the fit. The dotted and dot–dashed lines in Fig. 105.18(b) are the distributions predicted from the 2-D and 3-D models, respectively (presented in Ref. 27). The 3-D model prediction is in better agreement with the experimental results, as expected. It was shown[28] that the modulation $\sigma_{\rm rms}$ grows as $\alpha_\sigma g t^2$, as expected in a self-similar regime, where g is the foil acceleration, t is the time, and α_σ = 0.027±0.003 is a measured constant. The bubble-front amplitude h_b can be estimated[18] as $h_b \sim \sqrt{2}\,\sigma_{\rm rms}$, which yields $h_b \sim 0.04\ gt^2$. It was shown in Refs. 20 and 39 that Haan's saturation at amplitudes $S_k = 2/Lk^2$ in Fourier space is equivalent to self-similar growth $h_b = 0.04\ gt^2$ in real space. Therefore, experimentally measured growth is in agreement with what was predicted.[20,39] The weak, logarithmic dependence of the α_σ on the initial conditions[17] still requires experimental verification for ablative acceleration.

The experimental results presented above show the behavior of "average" modulation characteristics. The evolution of the average amplitude (calculated by the azimuthal average of the 2-D Fourier image) was compared with Haan's model predictions in Fourier space. The analysis in real space was presented in terms of bubble size distributions. The measured data, however, can also be used to quantitatively describe what happens to an individual bubble (in real space) and individual Fourier mode (in Fourier space). Figure 105.19 shows images of the modulation growth at the same area of the target measured at 2.7, 3.5, and 4.3 ns in the shot with a 35-μm-thick target driven at an intensity of ~5×10^{13} W/cm^2.

Figure 105.20 shows overlapped bubble contours of the 2.7- (gray lines) and 4.3-ns (black lines) images. As evident from this figure, some bubbles coalesce with others to form larger bubbles. Some bubbles disappear and other bubbles expand to take their place, while some bubbles stay in their original place without changing sizes. As for the Fourier-space analysis, if all modes at any wavelength grow uniformly according to Haan's model prediction for the average modulation growth, there could not be a bubble merger in real space. Therefore, to be consistent with the bubble-merger picture of real-space evolution, the individual Fourier modes at a given

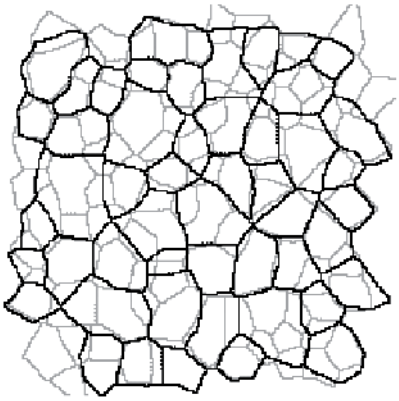
E14081JR

Figure 105.20
Bubble edge contours of the 2.7-ns (gray contours) and (c) 4.3-ns (black contours) images from Fig. 105.19. Some of the bubbles do not change their size while most bubbles merge into bigger bubbles and some bubbles disappear during evolution.

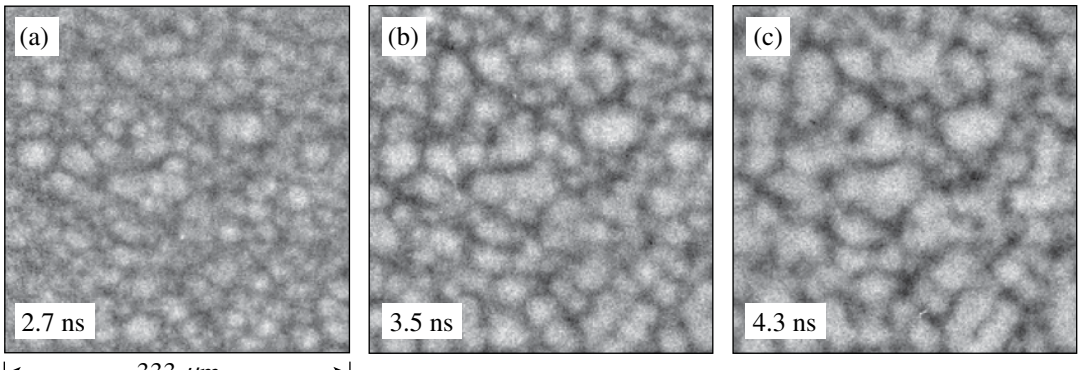

E14080JR

Figure 105.19
The evolution of the same target area as shown by the central parts (with a 333-μm analysis box size) of the x-ray framing-camera images measured at (a) 2.7 ns, (b) 3.5 ns, and (c) 4.3 ns in a 35-μm-thick target driven by a 12-ns laser pulse at an intensity of ~5×10^{13} W/cm^2. The evolution of each modulation feature can be tracked in these images.

(mainly short) wavelength should have a different growth than their average amplitude. Figure 105.21(a) shows the Fourier image with typical "spiky" amplitudes, characteristic to "noise-like" 3-D modulations. The azimuthal lineout of data at a 60-μm wavelength is shown in Fig. 105.21(b). There are many modes in this lineout and their average amplitude grows according to Haan's model prediction, as shown above. Is the growth of each individual mode in this lineout the same as the growth of the average amplitude? If it is the same, then the phase of each mode (related to the ratio of the real and imaginary parts of the mode's complex amplitude) does not change in time. Figure 105.21(c) shows the evolution of the absolute values of modes in a 60-μm wavelength lineout from 2.7 to 3.5 ns, while the evolution of the modes in a 20-μm wavelength lineout is presented in Fig. 105.21(d). These data show that all 60-μm wavelength modes grow similarly, while modes at a 20-μm wavelength do not all grow the same way and many phase changes are seen during the growth of these short-wavelength modes. Figure 105.21(e) shows the histograms of the absolute values of the phase changes of all modes at spatial wavelengths of 20, 30, and 60 μm measured between 3.5- and 2.7-ns images. At wavelengths of 30 and 60 μm, most of the modes do not change phases, while most of the modes at wavelengths of 20 μm change their phases significantly. As a result, the bubble merger in Fourier space corresponds to short-wavelength modes growing nonuniformly (with many modes changing their phases significantly), while longer-wavelength modes do not change their phases, meaning that the images keep their long-wavelength structure unchanged.

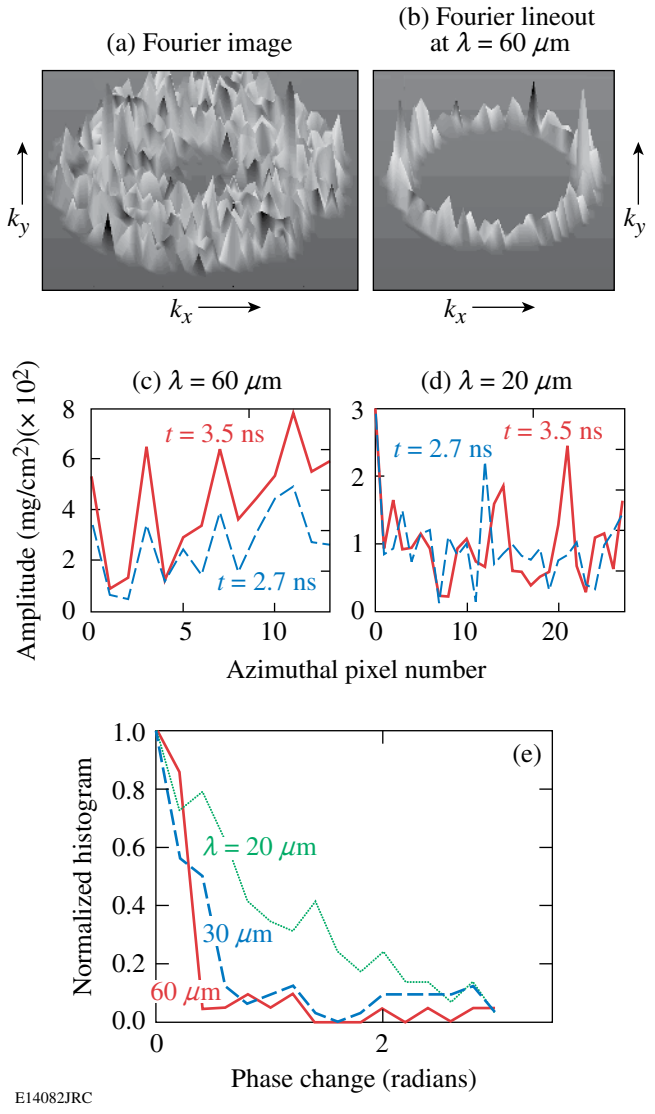

Figure 105.21
(a) An example of the typical measured Fourier-space image (shown in terms of the absolute value). (b) The azimuthal lineout of this image at a spatial wavelength of 60 μm. The azimuthal lineouts of absolute values of Fourier modes at a (c) 60-μm wavelength and a (d) 20-μm wavelength measured at 2.7 and 3.5 ns. (e) Normalized (to the value at zero phase change) histograms of the absolute phase change of the modes at spatial wavelengths of 20, 30, and 60 μm calculated from the difference of the 2.7- and 3.5-ns images. The bubble merger in Fourier space corresponds to the short-wavelength modes growing nonuniformly (with many modes changing their phases significantly), while longer-wavelength modes do not change their phases.

Conclusions

The nonlinear Rayleigh–Taylor growth of 3-D nonuniformities was measured near saturation levels using x-ray radiography in laser-driven planar foils. The initial target modulations were seeded by laser nonuniformities. The measured modulation Fourier spectra and nonlinear growth velocities are in excellent agreement with Haan's model[18] predictions in Fourier space.[25,26] These spectra and growth velocities are insensitive to initial conditions. Bubble competition and merger was quantified by the evolution of bubble size distributions in real space. A self-similar evolution of these distributions was observed.[28]

ACKNOWLEDGMENT

This work was supported by the U.S. Department of Energy Office of Inertial Confinement Fusion under Cooperative Agreement No. DE-FC52-92SF19460, the University of Rochester, and the New York State Energy Research and Development Authority.

REFERENCES

1. Lord Rayleigh, Proc. London Math Soc. **XIV**, 170 (1883).
2. G. Taylor, Proc. R. Soc. London Ser. A **201**, 192 (1950).
3. J. D. Lindl, Phys. Plasmas **2**, 3933 (1995).

4. B. A. Remington *et al*., Phys. Plasmas **4**, 1994 (1997).
5. K. S. Budil *et al*., Phys. Rev. Lett. **76**, 4536 (1996).
6. H. Takabe *et al*., Phys. Fluids **28**, 3676 (1985).
7. R. Betti, V. N. Goncharov, R. L. McCrory, P. Sorotokin, and C. P. Verdon, Phys. Plasmas **3**, 2122 (1996).
8. K. Shigemori *et al*., Phys. Rev. Lett. **78**, 250 (1997).
9. S. G. Glendinning, S. N. Dixit, B. A. Hammel, D. H. Kalantar, M. H. Key, J. D. Kilkenny, J. P. Knauer, D. M. Pennington, B. A. Remington, R. J. Wallace, and S. V. Weber, Phys. Rev. Lett. **78**, 3318 (1997).
10. C. J. Pawley *et al*., Phys. Plasmas **6**, 565 (1999).
11. J. P. Knauer, R. Betti, D. K. Bradley, T. R. Boehly, T. J. B. Collins, V. N. Goncharov, P. W. McKenty, D. D. Meyerhofer, V. A. Smalyuk, C. P. Verdon, S. G. Glendinning, D. H. Kalantar, and R. G. Watt, Phys. Plasmas **7**, 338 (2000).
12. T. Sakaiya *et al*., Phys. Rev. Lett. **88**, 145003 (2002).
13. B. A. Remington *et al*., Phys. Fluids B **5**, 2589 (1993).
14. K. I. Read, Physica **12D**, 45 (1984).
15. D. H. Sharp, Physica **12D**, 3 (1984).
16. M. B. Schneider, G. Dimonte, and B. Remington, Phys. Rev. Lett. **80**, 3507 (1998).
17. G. Dimonte, Phys. Rev. E **69**, 056305 (2004).
18. S. W. Haan, Phys. Rev. A, Gen. Phys. **39**, 5812 (1989).
19. S. W. Haan, Phys. Fluids B **3**, 2349 (1991).
20. D. Ofer, U. Alon, D. Shvarts, R. L. McCrory, and C. P. Verdon, Phys. Plasmas **3**, 3073 (1996).
21. C. L. Gardner *et al*., Phys. Fluids **31**, 447 (1988).
22. Q. Zhang, Phys. Lett. A **151**, 18 (1990).
23. J. Glimm and X. L. Li, Phys. Fluids **31**, 2077 (1988).
24. U. Alon *et al*., Phys. Rev. Lett. **74**, 534 (1995).
25. V. A. Smalyuk, T. R. Boehly, D. K. Bradley, V. N. Goncharov, J. A. Delettrez, J. P. Knauer, D. D. Meyerhofer, D. Oron, and D. Shvarts, Phys. Rev. Lett. **81**, 5342 (1998).
26. V. A. Smalyuk, O. Sadot, J. A. Delettrez, D. D. Meyerhofer, S. P. Regan, and T. C. Sangster, Phys. Rev. Lett. **95**, 215001 (2005).
27. D. Oron *et al*., Phys. Plasmas **8**, 2883 (2001).
28. O. Sadot, V. A. Smalyuk, J. A. Delettrez, D. D. Meyerhofer, T. C. Sangster, R. Betti, V. N. Goncharov, and D. Shvarts, Phys. Rev. Lett. **95**, 265001 (2005).
29. V. A. Smalyuk, T. R. Boehly, D. K. Bradley, V. N. Goncharov, J. A. Delettrez, J. P. Knauer, D. D. Meyerhofer, D. Oron, D. Shvarts, Y. Srebro, and R. P. J. Town, Phys. Plasmas **6**, 4022 (1999).
30. T. R. Boehly, D. L. Brown, R. S. Craxton, R. L. Keck, J. P. Knauer, J. H. Kelly, T. J. Kessler, S. A. Kumpan, S. J. Loucks, S. A. Letzring, F. J. Marshall, R. L. McCrory, S. F. B. Morse, W. Seka, J. M. Soures, and C. P. Verdon, Opt. Commun. **133**, 495 (1997).
31. Y. Lin, T. J. Kessler, and G. N. Lawrence, Opt. Lett. **20**, 764 (1995).
32. V. A. Smalyuk, V. N. Goncharov, T. R. Boehly, D. Y. Li, J. A. Marozas, D. D. Meyerhofer, S. P. Regan, and T. C. Sangster, Phys. Plasmas **12**, 040702 (2004).
33. V. A. Smalyuk, V. N. Goncharov, T. R. Boehly, J. A. Delettrez, D. Y. Li, J. A. Marozas, A. V. Maximov, D. D. Meyerhofer, S. P. Regan, and T. C. Sangster, Phys. Plasmas **12**, 072703 (2005).
34. S. V. Weber, S. G. Glendinning, D. H. Kalantar, M. H. Key, B. A. Remington, J. E. Rothenberg, E. Wolfrum, C. P. Verdon, and J. P. Knauer, Phys. Plasmas **4**, 1978 (1997).
35. V. N. Goncharov, S. Skupsky, T. R. Boehly, J. P. Knauer, P. McKenty, V. A. Smalyuk, R. P. J. Town, O. V. Gotchev, R. Betti, and D. D. Meyerhofer, Phys. Plasmas **7**, 2062 (2000).
36. S. P. Regan, J. A. Marozas, J. H. Kelly, T. R. Boehly, W. R. Donaldson, P. A. Jaanimagi, R. L. Keck, T. J. Kessler, D. D. Meyerhofer, W. Seka, S. Skupsky, and V. A. Smalyuk, J. Opt. Soc. Am. B **17**, 1483 (2000).
37. T. R. Boehly, V. A. Smalyuk, D. D. Meyerhofer, J. P. Knauer, D. K. Bradley, R. S. Craxton, M. J. Guardalben, S. Skupsky, and T. J. Kessler, J. Appl. Phys. **85**, 3444 (1999).
38. L. Vincent and P. Soille, IEEE Trans. Pattern Anal. Mach. Intell. **13**, 583 (1991).
39. M. J. Dunning and S. W. Haan, Phys. Plasmas **2**, 1669 (1995).